

de Haas—van Alphen measurements of the Fermi surface in ordered Cu_3Au

P. P. Deimel* and R. J. Higgins

University of Oregon, Physics Department, Eugene, Oregon 97403

(Received 31 December 1981; revised manuscript received 16 March 1982)

We report the observation of de Haas—van Alphen oscillations in ordered Cu_3Au . Data were taken in fields up to 90 kG and temperatures between 0.9 and 1.3 K. The results obtained are in very good agreement with a recent band-structure calculation. The shape of the closed electron piece in the fourth Brillouin zone was determined exactly by using the inversion scheme developed by Mueller *et al.* The radius of the neck orbit, which appears again remapped in the fourth Brillouin zone, is in surprising agreement with the rigid-band value. The superlattice band gap is approximately 0.04 Ry. Since large sections of the Fermi surface are close to the superlattice zone planes, a charge-density-wave-like mechanism could well be responsible for the order-disorder transformation.

I. INTRODUCTION

Over the past twenty years several efforts have been made to measure the change of the Fermi surface (FS) which occurs in the order-disorder transformation of Cu_3Au . During the ordering, the gold atoms pick out one of the four simple cubic sublattices which make up the fcc lattice. This creates a new periodicity, with the effect that new Brillouin-zone (BZ) boundaries are introduced in reciprocal space. Figure 1 shows how the FS of Cu_3Au in the disordered state may get divided by the new Brillouin-zone boundaries. This model FS of disordered Cu_3Au was constructed using 75% of the magnitude of the coefficients for copper and 25% of the corresponding coefficients of gold in the expansion formula given by Halse.¹ If this model is correct, the result of remapping the FS into the new BZ shows a closed hole sheet in the second BZ and multiply-connected electron "jungle gyms" in the third and fourth BZ.

Experiments have been performed that may reflect the electronic structure of ordered Cu_3Au . These include measurement of the Hall effect,² magnetic susceptibility,³ specific heat,⁴ thermoelectric power,⁵ Debye-Waller factor,⁶ x-ray scattering,⁷ and optical reflectivity.⁸ None of these methods, however, allows a direct measurement of the FS. Dramatic changes have been observed in the Hall effect when order sets in.² The Hall constant *changes sign*, consistent with the speculation that there is a hole sheet in the second BZ. Magnetic susceptibility³ and thermoelectric power measurements⁵ show a marked change when the temperature drops below the critical temperature of

388°C, suggesting density of states singularities. On the other hand, the specific heat⁴ changes by only 3.5%, suggesting that the total density of states at the Fermi level does not change much.

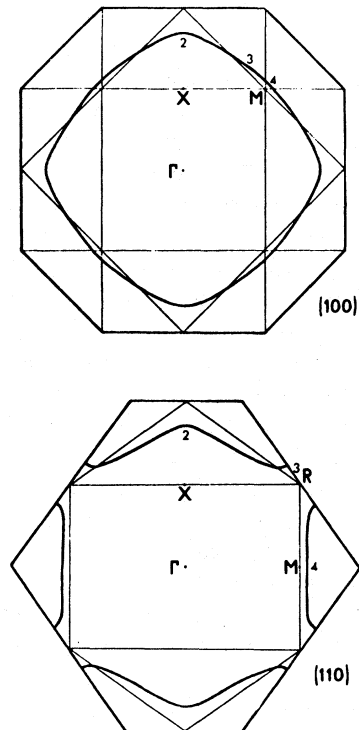


FIG. 1. Zero-gap coherent potential Fermi surface for Cu_3Au . Band labelings 2,3,4 are for the FS remapped into the Cu_3Au BZ. The labeling of points is for the simple cubic (ordered) BZ, for comparison with Fig. 3.

Although positron annihilation can in principle map an alloy Fermi surface, in practice the measurements⁹ on ordered Cu₃Au can just barely resolve the gross features of the noble-metal necks, and shed no light on the smaller perturbation caused by the ordered BZ faces.

The Cu-Au system is, of course, a classic in order-disorder studies. In equiatomic CuAu, for example, an extra incommensurate superlattice periodicity occurs whose variation with electron concentration has been associated¹⁰ with Fermi-surface-BZ interactions, an early example of charge density waves. We note in Fig. 1 large flat regions of FS close to the extra BZ planes of the ordered phase of Cu₃Au as well. Noble-noble metal alloys are also a good prototype for concentrated-alloy band theory, since the FS of the constituents are so well known and also so similar that complications due to charge transfer or other hybridization effects will not complicate the interpretation, as in ordered CuZn or in many intermetallic compounds.¹¹ Thus there is ample reason for wanting to know the FS of ordered Cu₃Au: to explain the peculiar bulk properties, as a prototype system for electronic contributions to order-disorder, and for alloy band theory in general.

To observe de Haas-van Alphen (dHvA) signals in ordered Cu₃Au, four different material problems had to be solved. First, single crystals had to be grown. Second, the stoichiometry had to be as perfect as possible, since off-stoichiometric atoms pile up in the antiphase domain boundaries and thereby limit the maximum obtainable ordered domain size. Third, the average domain size had to be large enough (at least several thousand angstroms) to allow the electrons to complete their orbits in the magnetic field. If the domains are too small, electrons may scatter off the domain walls, decreasing the dHvA signal amplitude. Fourth, the long-range order parameter had to be close to one. This parameter describes the percentage of gold atoms on their proper sublattice. In an ordered domain, every gold atom on the wrong sublattice acts as an impurity and therefore as a scatterer.

The dHvA signal amplitude is proportional to $\exp(-2\pi r/\omega_c \tau)$ which can be rewritten as $\exp(-\lambda \mu X/H)$. Here, r is the dHvA harmonic index, ω_c the cyclotron resonance frequency, τ the mean orbitally averaged scattering time, λ is a constant equal to 146.9 kG/K, μ is the ratio of the effective electron mass to the free electron mass, X is the Dingle temperature in K, and H is the magnet-

ic field in kG. For a field of 100 kG and a mass ratio μ equal to one, the Dingle temperature cannot be larger than a few K for the dHvA signal still to be detectable. Data¹² show that an impurity concentration of 1 at. % Au in Cu amounts to a Dingle temperature of 16 K. This places restrictions on both the stoichiometry and on the order parameter S . By carefully weighing the starting material, the stoichiometry could be controlled to within less than 0.1%, and was in practice not the dominant problem. Assuming that a similar relationship between Dingle temperature and impurity concentration holds for the concentrated alloy, it is obvious that less than one percent of the Au atoms should be on the wrong sublattice. This means that S has to be 0.99 or better.

X-ray scattering experiments give some understanding about the size of the ordered domains and the long-range order parameter as a function of the annealing time and temperature.⁷ The average diameter of the ordered domains grows with the square root of time. Data show that at an annealing temperature of 375 °C an average domain size of 10⁴ Å is reached after about seven months.⁷ Data for the long-range order parameter S show that annealing temperatures down to 200 °C are necessary to reach a value for S which is close to one.¹³

II. MATERIALS PREPARATION

Five single crystals have been grown, each one with a slightly different initial stoichiometry. Copper and gold have different vapor pressures and therefore more copper than gold is lost during the crystal-growing process. The amount of the lost material could not be determined to better than 0.1%, and therefore this hit-or-miss approach seemed to be most appropriate. The starting material was 99.9999% pure copper and gold. The samples were homogenized for several hours in vacuum at 1100 °C. A conventional Bridgman system was used for the crystal-growing process. To ensure that no concentration gradient occurred, several pieces along the sample rod were cut. A microanalysis using an x-ray fluorescence probe and standard reference materials from National Bureau of Standards showed no concentration gradient within the limit of detectability (0.4%). After orienting and spark-cutting the single crystals, they were etched in a solution of 10% NaCN and 10% (NH₄)₂SO₈ (Ref. 14). To remove any

damage in the samples which might have occurred during the cutting process, all the samples were annealed at 900°C for two days.

The long-term annealing was done in two stages. First, the samples were annealed at a temperature as close as possible to T_c to increase the size of the ordered domains at the maximum rate. Second, a slow cool-down process followed, proceeding down to temperatures low enough to attain the desired order parameter. For the long-term annealing process the samples were packed in high-purity quartz wool and vacuum-sealed in quartz glass ampoules. The samples were heated to 540°C and then cooled to about 400°C. From there the temperature was slowly decreased through T_c until a temperature of 375°C was reached. This slow-cooling process lasted for about ten days. For the next seven and one-half months the temperature stayed at 375°C. Extrapolating from known data,⁷ this much time was necessary to reach average domain sizes of the order of 10^4 Å. Domains of this size are necessary to accommodate the hole orbit in the (100) plane, whose average radius in k space is estimated to $1.2 \times 10^8 \text{ cm}^{-1}$ at a field of 80 kG. After that, a cool-down strategy was designed to increase the long-range order parameter.

Since there is no known explicit functional relationship between the long-range order parameter S and the annealing time t at a given temperature T , the assumption was made that S shows a diffusion-type behavior:

$$S = S_{\text{equ}}(T)(1 - e^{-ct}),$$

$$c = c_0 e^{-Q/k_B T},$$

where c is the time constant, Q is the activation energy (2 eV), and $S_{\text{equ}}(T)$ is the equilibrium value for S . The values for c_0 , Q , and $S_{\text{equ}}(T)$ were taken from Feder *et al.*¹³ It can be seen from the time constant that S initially grows faster with increasing temperature, but at the same time the equilibrium value for S decreases (Fig. 2). Thus, to achieve the largest value for S in the shortest time, the rate of change of S as a function of time t and temperature T as parameter was calculated from the above equation. At whatever point in time the growth rate of S at a given temperature becomes less than the rate at a slightly lower temperature, the annealing procedure was continued at this lower temperature, which insures a faster rate than before. This cooling process lasted for another seven months and involved the reduction in temperature in steps of 10°C down to 190°C. The

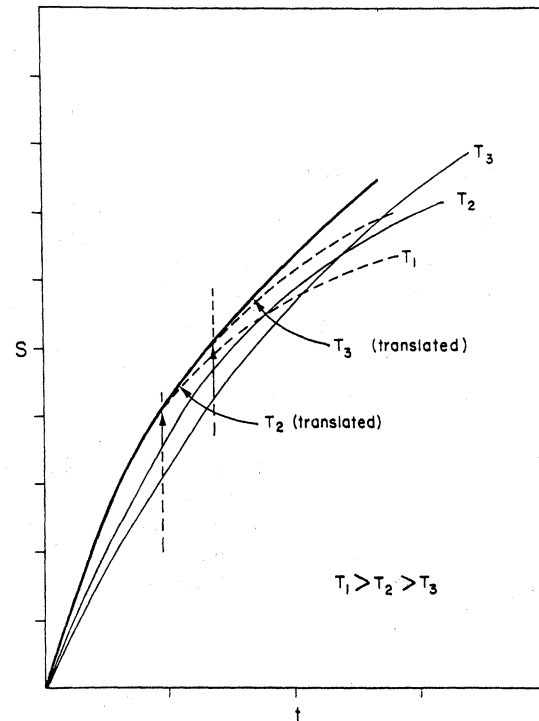


FIG. 2. Long-range order parameter S vs time t with temperature T as parameter (schematically). For higher temperatures, S initially grows faster but reaches a smaller equilibrium value later. The heavy line shows the envelope curve for the fastest growth of S vs time.

residual resistivity ratio (RRR) of the best sample had a value of 8.8. The RRR was measured by using a contactless method.¹⁵

III. RESULTS AND DISCUSSION

A. Cu_3Au FS from band-structure calculations

The first *ab initio* band-structure calculation in Cu_3Au was performed using both the modified and the orthogonalized-plane-wave method and a muffin-tin potential.¹⁶ The resulting FS looks similar to the one which is obtained by remapping a Cu_3Au FS. More recent calculations, based on optical spectra of ordered Cu_3Au , were done using relativistic linear muffin-tin orbitals.¹⁷ The FS thus obtained is similar to the one from Gray and Brown,¹⁶ the primary difference being that the electron sheet in the fourth BZ is disconnected in Skriver and Lengkeek's¹⁷ calculation (Fig. 3).

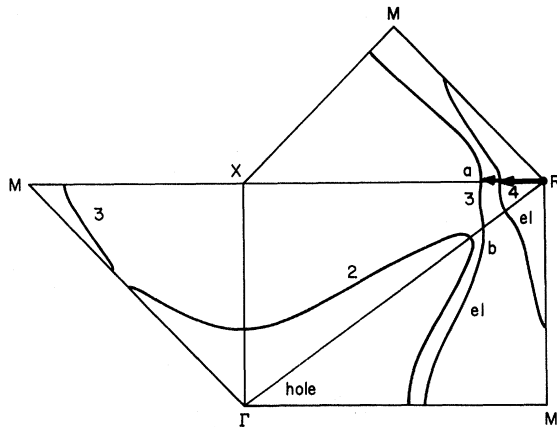


FIG. 3. Fermi-surface model obtained from RLMT0 calculations consistent with optical absorption experiments (Ref. 17). The band labeling is as in Fig. 1. The arrows show points in the third and fourth zone that originate from the neck in the disordered state.

B. Cu_3Au FS obtained by remapping

We will use the predictions of the remapped FS as a guide to topology and an estimate of relative sizes of orbits. The superlattice band gap will alter the expected values and perhaps the topology, allowing the gap to be estimated.

A program was written to draw the cross sections of a weighted FS from the known FS of copper and gold. The formula and the coefficients used are given by Halse.¹ The weighted FS was constructed by using 75% of every coefficient for copper and adding to it 25% of the corresponding coefficient for gold. This approach is physically preferable to the alternative of averaging FS radius vectors, which leads to scaling problems (due to the 10% difference in lattice parameter between Cu and Au) and a large uncertainty in the size of small orbits where the Fermi surface just overlaps a Brillouin-zone boundary (BZB). The new BZB introduced by the superlattice cause a complete change in the topology of the original Cu_3Au FS (Fig. 1). The first BZ is totally full. The second BZ contains a closed hole sheet at the center of the BZ (Fig. 4). The faces of the cube come from the areas around the [100] directions of the original disordered FS. The third BZ contains an extended electron sheet that shall be referred to as a jungle gym (Fig. 4). Its centers or junctions lie at the corners of the BZ. The arms stretch along the edges of the BZ and their shape is ellipsoidal. These pieces originate from sections which connect



FIG. 4. Remapped FS of Cu_3Au . The second BZ contains a hole sheet (top). The third (middle) and fourth (bottom) BZ contain electron sheets. The length of an edge of the BZ is $0.267(2\pi/\text{\AA})$.

adjacent necks of the disordered FS. This piece of the FS which is in the fourth BZ is also a jungle gym (Fig. 4), but the arms are much thinner and more like tubes compared to the ones in the third zone.

Figure 5 shows the original FS in the disordered state and the sections which make up the FS in the ordered state. The part of the FS enclosed by the dotted line contributes to the hole sheet in the second BZ. The sections between the dashed lines belong to the jungle gym in the fourth BZ. It can be seen that the neck will appear again at the arm junctions in a plane perpendicular to the [111] direction. The pieces that make up the jungle gym in the third BZ lie between the dotted and the dashed lines. From the remapping procedure, it is not straightforward to estimate the area one would get by cutting the junctions perpendicular to the [111] direction.¹⁸ For clarity's sake only a few pieces have been drawn, but using symmetry it is

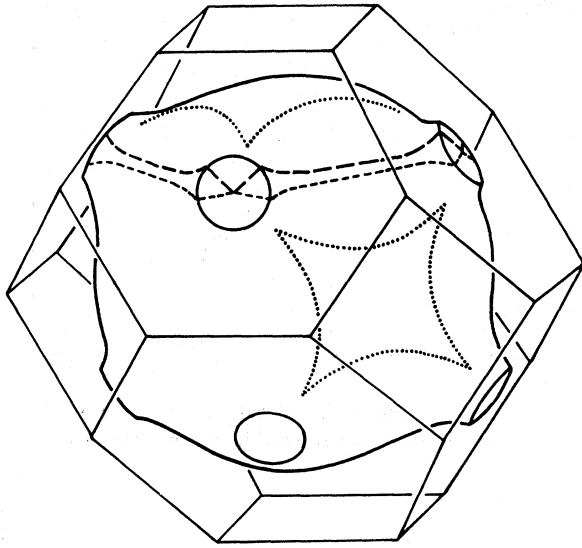


FIG. 5. FS of disordered Cu_3Au . The dotted line encloses the section that makes up the hole sheet in the second BZ. Sections between the dashed lines contribute to the electron sheet in the fourth BZ. Sections between the dashed and dotted lines make up the electron sheet in the third BZ.

fairly obvious where the other pieces come from.

In Table I a summary is given of the frequencies expected from remapping in the major symmetry directions. The dHvA frequency F is expressed in terms of the area A in reciprocal space as $F = (hc/e)A$ with hc/e as the flux quantum.

C. Experimental results

All the measurements were performed at temperatures between 0.9 and 1.3 K and fields up to 90 kG using the field modulation technique.¹⁹ The results are shown in Figs. 6 and 7. The various branches are labeled to identify the individual frequencies. Branches a and b can be assigned to the arms of the jungle gym in the third BZ. Contrary to what one would expect from the ellipsoidal shape in both the remapped FS (Fig. 4) and also in the band calculation (Fig. 3), this piece is slightly hyperboloidal. The area rises more rapidly than that of a cylinder (dashed line in Fig. 6). This is consistent with our observation of only one frequency, since the noncentral extremum vanishes if the principal cross section has become a minimum ($d^2A/dP_z^2 > 0$) rather than a maximum. The signal was observed in the (100) plane up to an angle of 48° . The disappearance is abrupt (within 2°); the extremum has vanished. A third branch, labeled c , also belongs to the jungle gym in the third BZ. The frequency of the arms changes little when the field is tipped out of the (100) plane away from the [110] direction. Branches d in the (100) plane and e in the (110) plane belong to a closed sheet in the fourth BZ. Contrary to what one obtains from simple remapping, the junctions of the jungle gym in the fourth BZ are disconnected. A unique solution exists²⁰ for the inversion of cross-section areas into radius vectors, provided that the surface is closed, has single-value radius vectors, and has a center of inversion symmetry. We use a set of cu-

TABLE I. Frequencies expected from remapping in the major symmetry directions. Numbers are in units of MG; max and min refer to maximum and minimum, respectively. The hole orbits in the third and fourth BZ traversing four junctions should be between 200 and 250 MG.

BZ	Directions		
	[100]	[110]	[111]
2nd	central min: 50 noncentral max: 180	central max: 147	
3rd	central max (center of arms): 15 noncentral min (between center of arms and junction): 5	central max (center of arms): $\lesssim 21$	central max: $\lesssim 21$
4th	central min (center of arms): 2.7	central min (center of arms): 3.8	arm junction (equivalent to "neck"): 20 central min: 4.7

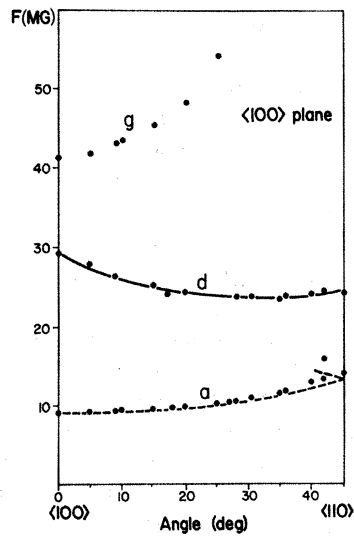


FIG. 6. Measured dHvA frequencies vs angle in the (100) plane. The solid line shows the calculated area using Mueller's inversion scheme for the closed electron sheet in the fourth zone. Branches *a, d, g* belong to the third, fourth, and second BZ, respectively.

bic harmonics ${}_i K_l$ to fit the areas obtained by experiment, thereby determining the expansion coefficients²¹ ${}_i b_l$:

$$A(\theta, \rho) = \sum_{i,l} {}_i b_l {}_i K_l(\theta, \rho).$$

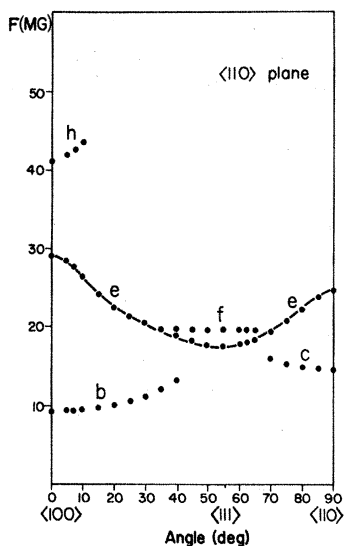


FIG. 7. Measured dHvA frequencies vs angle in the (110) plane. The solid line shows the calculated area using Mueller's inversion scheme for the closed electron sheet in the fourth zone. Branches *b, c, and f* belong to the third zone, *h* to the second, and *e* to the fourth zone.

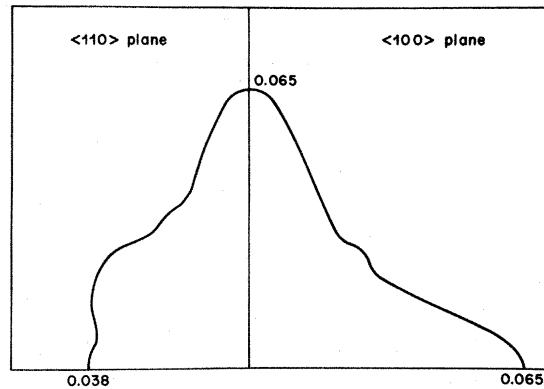


FIG. 8. Polar plot of the closed electron sheet in the fourth BZ. Numbers for the radius vectors are in units of $(2\pi/\text{\AA})$.

The relationship between the expansion coefficients ${}_i b_l$ and the square of the radius vector is²²

$$k^2(\theta, \rho) = \sum_{i,l} {}_i b_l [\pi P_l(0)]^{-1} {}_i K_l(\theta, \rho).$$

In this expansion only even l appear, since the Legendre polynomials $P_l(0)$ are zero for odd l . Figures 8 and 9 show the calculated radius vectors²³ on a polar plot and a k vs θ plot, respectively. The program is written so that a cross-comparison is made between the measured areas and the areas one would get using the calculated radii. The error thus obtained from the root-mean-square deviation amounts to less than 1% compared to the smallest cross section. The largest single deviations range up to about 2.5%, com-

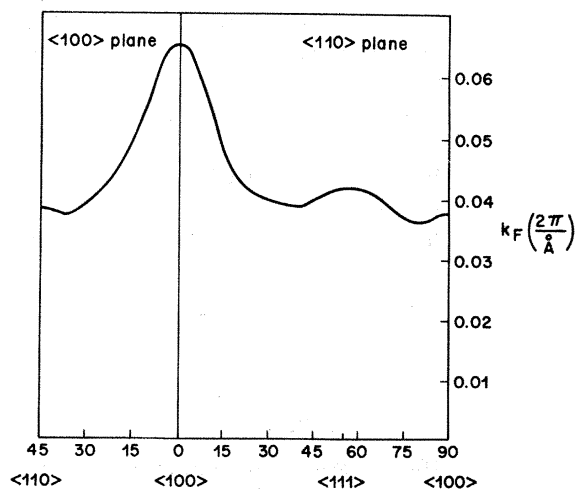


FIG. 9. Radius vector k vs angle of the electron sheet in the fourth BZ.

pared to the smallest cross section. Since these errors lie within the experimental error bars, one can be confident in the shape and size of this piece of FS.

Rotation diagrams are continuous and $dF/d\theta = \text{const}$ around 55° , which proves that the lower branch e belongs to the closed sheet rather than branch f (Fig. 7). Branch f probably comes from the junction of the jungle gym in the third BZ. This signal is observed only between 40° and 65° , because the extremal orbit runs up the arms when tilted away from the 55° axis. The number of electrons at the extremal area diminishes, therefore the signal vanishes abruptly. Even though this orbit is observed only over 25° , it is completely flat over that range. The junction looks more like a sphere, as in the band structure (Fig. 3) rather than being caved in, as in the remapped model (Fig. 4). Finally, the branches g and h in the (100) and (110) planes, respectively, belong to the closed hole sheet in the second BZ. At an angle of 25° in the (100) plane, the change in the extremal area is more than twice as much as if this piece were a cylinder. As expected from Fig. 3 and from remapping, this sheet is hyperboloidal at the [100] direction.

From the data, a FS for ordered Cu_3Au is proposed with the topology shown in Fig. 10. The hole sheet is 30% to 40% smaller than expected from remapping. Since the electron pieces of the FS in the third and fourth BZ are also smaller, electron states are shifted from the third and fourth BZ into the second.

The piece of FS in the third BZ (Fig. 10) has tubelike arms, which are only slightly hyperboloidal, and has spherical sections at the junctions. Also the cross section between the junctions is not as "pointed" at the edges as the remapped FS shows, simply because the signal can be observed up to an angle of about 48° away from [100]. The noncentral closed electron sheets in the fourth BZ (Fig. 10) have their "horns" extend to less than a quarter of the length of the BZ edge. In units of $2\pi/\text{\AA}$, the length of the horns is 0.065 compared to 0.267, the length of the BZ edge. A comparison of three radius vectors of the electron sheet in the fourth BZ obtained from experiment and from band-structure calculations¹⁷ (relativistic linear combination of muffin-tin orbitals) is shown in Table II [k vectors in units of $2\pi/\text{\AA}$, lattice constant equal to 3.747\AA (Ref. 13)].

The vectors along XR in Fig. 3 map back to the neck in the fcc BZ, and are thus a measure of the

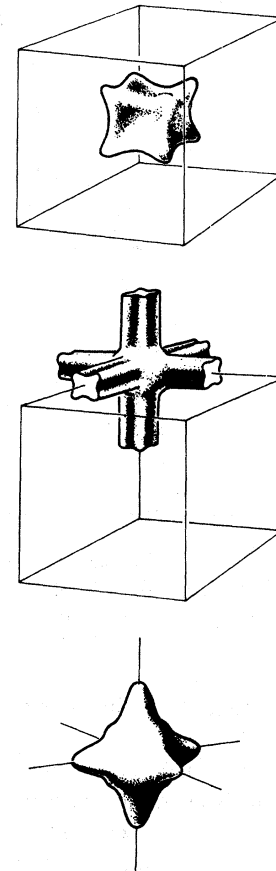


FIG. 10. Proposed FS models of the hole sheet in the second BZ (top) and the electron sheet in the third BZ (middle). The model for the noncentral closed electron sheet in the fourth BZ is shown in the bottom figure.

neck radius in the concentrated alloy. The radius vector calculated from the average of the areas in the third and fourth zones deviates from the radius in the concentrated alloy by only 4%.²⁴ The most significant difference between our data and the model proposed by Skriver and Lengkeek¹⁷ is that the jungle gym in the third BZ in our model is

TABLE II. Comparison of three radius vectors of the electron sheet in the fourth BZ obtained from experiment and band-structure calculations.

	Experiment	Band structure
[100]	0.065	0.088
[110]	0.038	0.027
[111]	0.042	0.030

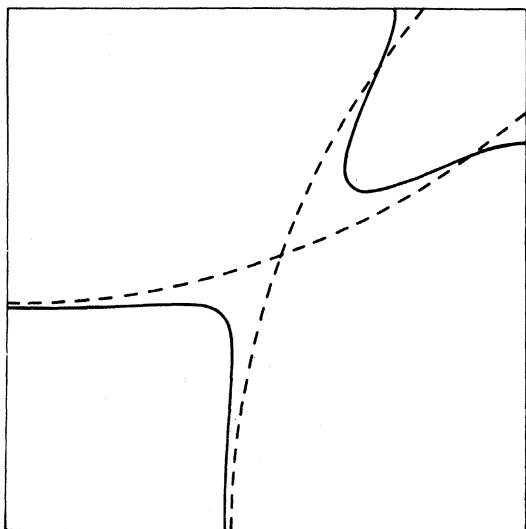


FIG. 11. Comparison of a Harrison construction NFE FS (dashed line) in the (100) plane with a FS obtained by first-order perturbation theory.

slightly hyperboloidal and in their model strongly ellipsoidal.

A first attempt was made to calculate the superlattice band gap from the measured dHvA frequencies in the (100) plane. The result is 0.04 Ry.²⁴ This value has been obtained by assuming that

$$A(\text{CPA}) - A(\text{obs}) = A(\text{NFE}) - A(\text{OPW}).$$

Here, CPA denotes coherent potential approximation, NFE denotes nearly free electron, and OPW denotes orthogonalized plane wave. The difference in cross-section areas of a Harrison construction nearly-free-electron FS [$A(\text{NFE})$] and the area obtained by turning on the superlattice band-gap energy in first-order perturbation theory [$A(\text{OPW})$] (Fig. 11) should balance the difference between the coherent potential $A(\text{CPA})$ and the actual observed cross sections $A(\text{obs})$. This comparison is made only for the point of near contact between second-zone holes and third-zone electrons in the (100) plane (see Fig. 1) which is split by the superlattice

band gap. $A(\text{CPA})$ was obtained from a weighed sum of a Cu and Au FS with the Fourier coefficients given by Halse.¹

In summary, the FS of Cu_3Au has been measured. Three pieces of FS have been identified: a cubelike hole orbit in the second BZ, an electron-like jungle gym with hyperboloidal arms and spherelike junctions in the third BZ, and noncentral closed electron pieces in the fourth BZ.

An estimate of the superlattice band gap has been made which we hope will encourage a calculation of the electronic contribution to the order-disorder transformation. Finally, the "neck radius" of Cu_3Au , determined unambiguously (using symmetry arguments) from the third and fourth zone cross sections at [111], is within 4% of the rigid band value.

ACKNOWLEDGMENTS

We would like to thank R. H. Hendel and D. E. Mikkola for helpful discussions during the initial stages of crystal growth, T. G. Matheson for valuable help during the experiments, and R. K. Goodall for supplying us with data for the energy gap. This research was supported by the National Science Foundation, Division of Materials Research, Grant No. GP78-73011.

APPENDIX

Effective masses have been measured: the 9.2-MG orbit at [100] ($\mu = 0.55 \pm 0.02$) and the 17.4-MG orbit at [111] ($\mu = 0.47 \pm 0.02$). The effective masses are in units of the free-electron mass. To determine the effective masses from the amplitudes, a least-squares fitting program was used and the function $[\sinh(x)]^{-1}$ instead of just $\exp(-x)$. The mass for the 41.5-MG orbit at [100] was also measured, but since only three data points were taken, its value of 0.69 should be taken with caution.

*Present address: Bell Laboratories, 600 Mountain Avenue, Murray Hill, NJ 07974.

¹M. R. Halse, *Philos. Trans. R. Soc. London Ser. A* **265**, 507 (1969).

²A. R. von Neida and R. B. Gordon, *Philos. Mag.* **7**, 1129 (1962).

³G. Airoldi and M. Drosi, *Philos. Mag.* **19**, 349 (1963).

⁴G. C. Kuczynski, M. Doyama, and M. E. Fine, *J. Appl. Phys.* **27**, 651 (1956).

⁵G. Airoldi, M. Asdente, and E. Rimini, *Philos. Mag.* **10**, 43 (1964); C. L. Foiles (unpublished).

⁶P. Bardhan and J. B. Cohen, *Acta Crystallogr. Sec. A*

- 32, 597 (1976).
- ⁷G. E. Poquette and D. E. Mikkola, *Trans. Metall. Soc. AIME* **245**, 743 (1969).
- ⁸W. Scott and L. Muldower, *Phys. Rev. B* **9**, 1115 (1974).
- ⁹H. Morinaga, *Phys. Lett.* **34A**, 384 (1971).
- ¹⁰H. Sato and R. S. Toth, *Phys. Rev.* **124**, 1833 (1961).
- ¹¹D. J. Sellmyer, in *Solid State Physics*, edited by H. Ehrenreich, F. Seitz, and D. Turnbull (Academic, New York, 1978), Vol. 33, p. 83.
- ¹²R. O. Paulsen, D. I. Randles, and M. Springford, *J. Phys. F* **4**, 981 (1974).
- ¹³R. Feder, M. Mooney, and A. S. Nowick, *Acta Metall.* **6**, 266 (1958).
- ¹⁴G. C. Kehl, *Principles of Metallographic Laboratory Practices* (McGraw-Hill, New York, 1949).
- ¹⁵W. Wejgaard and V. S. Tomar, *J. Phys. E* **7**, 395 (1974).
- ¹⁶D. Gray and E. Brown, *Phys. Rev.* **160**, 567 (1967).
- ¹⁷H. L. Skriver and H. P. Lengkeek, *Phys. Rev. B* **19**, 900 (1979).
- ¹⁸The radius vector of such an orbit in the (111) plane comes close to the original neck radius at point *a* in Fig. 3. Point *b* shows how far the arm junction extends outward along [111]. For the remapped case, *b* corresponds to the tips of the dotted pieces in Fig. 5.
- ¹⁹D. Shoenberg and P. J. Stiles, *Proc. R. Soc. London Ser. A* **281**, 62 (1964).
- ²⁰I. M. Lifshitz and A. V. Pogorelov, *Dokl. Akad. Nauk. SSSR* **96**, 1134 (1954).
- ²¹F. M. Mueller and M. G. Priestley, *Phys. Rev.* **148**, 638 (1966).
- ²²F. M. Mueller, *Phys. Rev.* **148**, 636 (1966).
- ²³Program provided by F. M. Mueller *et al.*
- ²⁴P. P. Deimel, R. J. Higgins, and R. K. Goodall, *Phys. Rev. B* **24**, 6197 (1981).